

Dielectric relaxation in metal-coated particles: the dramatic role of nano-scale coatings

I J Youngs^{1,3}, N Bowler², K P Lymer¹ and S Hussain¹

¹ Future Systems Technology Division, QinetiQ limited, Rm 1146, Bldg A7, QinetiQ Ltd, Ively Road, Farnborough, Hampshire, GU14 0LX, UK

² Center for NDE, Iowa State University, 279 ASC II, 1915 Scholl Road, Ames, Iowa 50011-3042, USA

E-mail: ijyoungs@dstl.gov.uk and shussain@QinetiQ.com

Received 30 June 2004

Published 6 January 2005

Online at stacks.iop.org/JPhysD/38/188

Abstract

Insulating materials filled with conducting particles permit tailoring of electrical, electromagnetic and thermal properties of the resulting composite. When the filler particles are small and metallic, a dielectric relaxation due to interfacial polarization is commonly observed at optical or smaller wavelengths. Here, experimental results are presented in which the dielectric relaxation is shifted to microwave frequencies as a result of using metal-coated dielectric particles with a nano-scale coating thickness. The results are analysed in the context of effective medium theory adapted for multi-layer particles. Such a large shift in relaxation frequency, compared with that for a similar composite with solid metal filler particles, is shown to be a function of both the coating geometry and a thin-film-related reduction in the conductivity of the metal. The observed broadening of the relaxation peak is attributed to non-uniformity of the coating thickness and a consequent distribution of coating conductivity.

(Some figures in this article are in colour only in the electronic version)

1. Introduction

Composites formed from a mixture of conducting particles in an insulating host medium are widely studied for tailored electrical or electromagnetic functionality [1]. In many applications, especially those related to use up to microwave frequencies, this functionality is determined by electrical conduction processes related to the formation of connected networks of conducting filler particles. The properties of such composites can be described using percolation theory [2, 3]. A percolating composite undergoes a dramatic insulator-to-conductor transition as the filler concentration is increased above some critical value that is well below the close-packing limit. At this critical concentration, known as the percolation threshold, the conductivity of the composite increases,

³ Present address: Physical Sciences Department, Dstl, Rm 14, Bldg 352, Porton Down, Salisbury, Wiltshire, SP4 0JQ, UK.

possibly by many orders of magnitude. Furthermore, in this transition region both the real and imaginary components of permittivity are highly dispersive over a broad frequency range. The high frequency limit to this dispersion is set by the interfacial polarization (or Maxwell–Wagner–Sillars) relaxation frequency [4]. For conductor–insulator composites, this limiting frequency is determined primarily by the conductivity of the filler. For metallic fillers the interfacial relaxation is observed well into the optical region of the spectrum [5]. It is this relaxation process that is the subject of this paper.

The design of composite materials with prescribed electromagnetic properties is hindered by the fact that it is difficult to accurately parametrize the complex dielectric response of a composite experimentally. This is because the critical dielectric features of the system, one of which is the interfacial relaxation, are commonly distributed over a very

wide region of the frequency spectrum (perhaps from dc to light). There is no single instrument or sample geometry that can be used to capture the dielectric response over the entire spectrum, even though measurements from $\sim 10^{-5}$ to $\sim 10^9$ Hz are possible (see, e.g. [6]). A potential way around this characterization difficulty is to find fillers whose conductivity is lower than that of typical metals, so that the interfacial relaxation frequency is shifted into the microwave region and the composite material can be parametrized by standard means. In practice, however, the choice of filler conductivity is limited. Even the conductivity of graphitic carbons (e.g. carbon blacks, graphite powder), of the order of 10^5 S m^{-1} , is too high to produce relaxation at microwave frequencies. Certainly there is no continuum of conductivity readily available through naturally occurring materials. This paper presents the use of filler particles composed of nano-scale metal coatings on micron-scale dielectric particles as a means of observing dielectric relaxation at microwave frequencies. The experimental methods and results are described in sections 2 and 3. The relevant effective medium theory is described in the context of the experimental results in section 4. Section 5 explores the observed broadening of the relaxation peak in terms of distributions of the particle size and coating thickness. The conclusions are summarized in section 6.

2. Experimental methods

The particles studied are hollow glass micro-spheres (3M Scotchlite™ S60 glass microbubbles) coated with tungsten and then overcoated with a protective, insulating layer of

alumina [7]. The tungsten thickness is nominally 20 nm and the alumina thickness nominally 3 nm [8]. The alumina outer layer stabilizes the tungsten, preventing oxidation, and has the additional benefit of preventing percolation in the mixture. This means that the interfacial polarization process can be studied in isolation from conduction effects. The physical properties of the particles are summarized in table 1. The matrix material used consisted of paraffin wax flakes (Aldrich) with a density of 0.899 g cm^{-3} .

Master batches for composites with filler concentrations in the range 0–55 vol% were prepared by hand mixing pre-weighed quantities of the two components at a temperature above the melting point of the paraffin wax (about 60°C). The mixture was removed from the heat and mixing continued during cooling until the mix solidified. Test samples were subsequently prepared by cold-pressing pellets of appropriate cross-sectional dimensions at pressures of approximately $63 \pm 8 \text{ MPa}$ for the coaxial samples and $58 \pm 8 \text{ MPa}$ for the WG22 and WG24 waveguide samples. The pressure was applied for 30 s using a KBr press. These pressures were chosen to maximize consolidation and minimize trapped air whilst not exceeding the crush strength of the micro-bubbles.

The microwave complex permittivity of the composites was determined by measuring the complex reflection and transmission coefficients of a sample placed in a section of transmission line. A number of methods are available for measuring complex permittivity at microwave frequencies [15], the method used here being the reflection/transmission (RT) method described by Baker-Jarvis [16] with the assumption that the composites are non-magnetic. (The validity of this assumption was confirmed by first using

Table 1. Physical properties of coated particles.

Parameter	Value	Source/comment
Coated particle		
Density (g cm^{-3})	0.62	[8], value used in formulating composites
	0.539 ± 0.026	Measured by helium pycnometer
Crush pressure (MPa)	69	[7]
Core particle		
	Glass microbubble	3M™ Scotchlite™ S60
Density (g cm^{-3})	0.60	[9]
Mean radius (μm)	15	[9]
10th centile radius (μm)	7.5	[9]
90th centile radius (μm)	27.5	[9]
Shell material	Soda-lime-borosilicate glass	[9]
Shell density (g cm^{-3})	2.5	[10], estimated from values for A and E glass
Shell thickness (μm)	1.311	Calculated from particle and shell densities for mean particle size
Shell real permittivity	4.8	[11], Pyrex, 25°C , 10 GHz
Shell loss tangent ($\times 10^4$)	98	[11], Pyrex, 25°C , 10 GHz
Core material	Air	Assumed
Tungsten coating		
Thickness (nm)	20	[8], mean value
Bulk conductivity (S m^{-1})	$1.77e7$	[12]
Bulk plasma frequency, ω_p (eV)	7.6	[13], theoretical
Bulk relaxation time, τ_{bulk} (s)	$173.133/\omega_p$	Calculated from bulk conductivity
Bulk Fermi velocity, v_F (m s^{-1})	$9.6e5$	[14], theoretical
Alumina outer coating		
Thickness (nm)	3	[8]
Real permittivity	8.79	[11], Coors, 25°C , 10 GHz
Loss tangent ($\times 10^4$)	18	[11], Coors, 25°C , 10 GHz

the Nicholson–Ross–Weir (NRW) method [16] to derive both the complex permittivity and permeability of the samples from the same measured reflection and transmission coefficients. For non-magnetic materials, the RT method is preferred because it reduces measurement uncertainty and can improve loss resolution.) A 7 mm coaxial transmission line was used for measurements over the frequency range 1–18 GHz and a rectangular waveguide was used for measurements over the frequency ranges 33–40 GHz (WG22) and 40–60 GHz (WG24). Due to the different cross-sectional geometry for the two transmission line types, separate sets of test samples were required for the three frequency ranges. This leads to the possibility of a systematic shift between the data sets due to small differences in filler dispersion and the pressure applied during pelletization, despite the fact that the same master batch was used to make samples for each of the three frequency ranges.

The method for determining the measurement uncertainty for the coaxial system has been described elsewhere [17].

3. Experimental results

Figure 1 presents the measured dielectric response of paraffin wax over the frequency range 1–18 GHz. Values derived from both the NRW and RT methods are presented to demonstrate the improvement in measurement uncertainty that can be obtained by making the assumption that the material under test is non-magnetic, which is obviously true for this material. The measured values are in agreement with those reported by von Hippel [11] ($\epsilon_m = 2.25(1 - j2.5/10^4)$ at 10 GHz) and it is noted that the imaginary component is less than the typical resolution ($\sim \pm 0.05$) of this broadband measurement technique. It is noted that there is some ripple on the measured

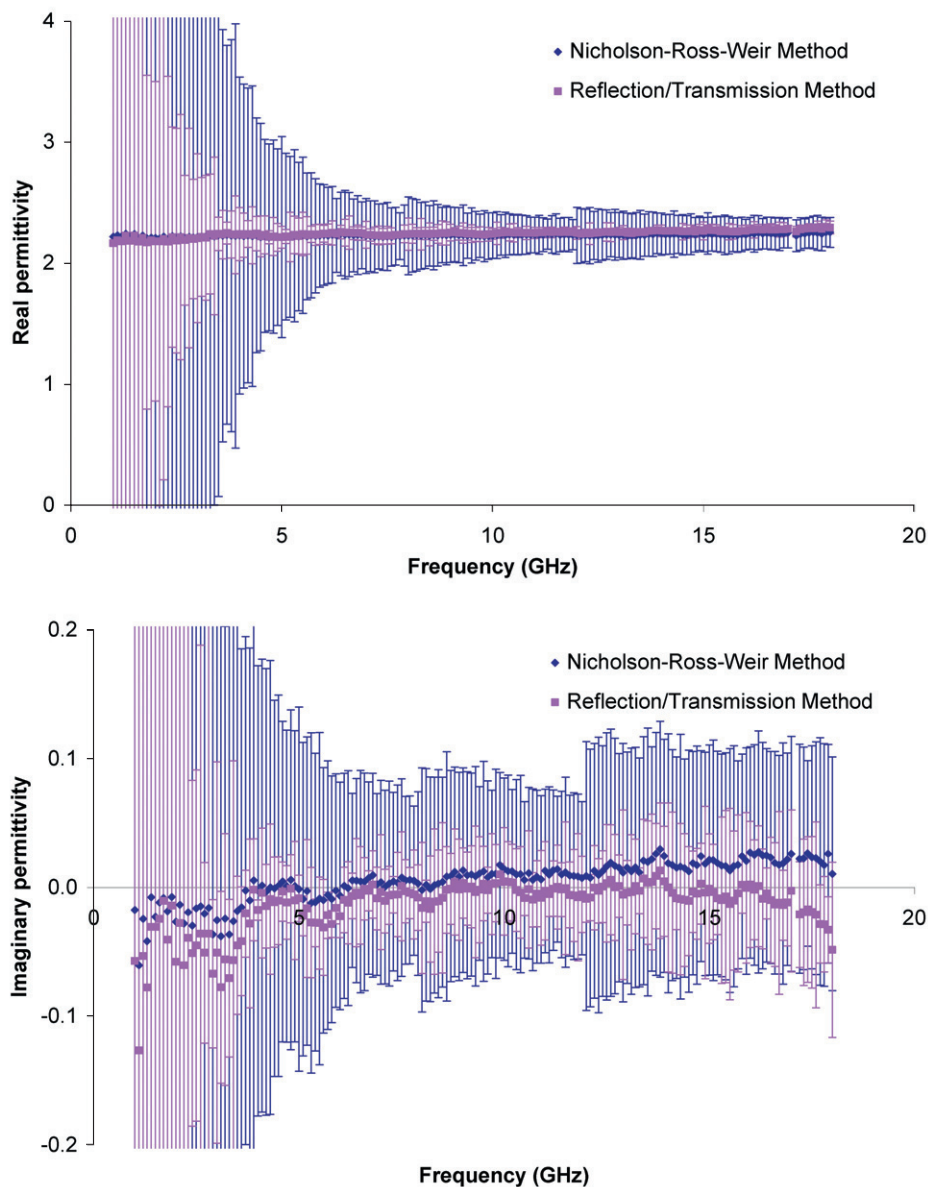


Figure 1. Real and imaginary components of the permittivity for paraffin wax, derived from measured reflection and transmission coefficients with (RT method) and without (NRW method) the assumption that the material is non-magnetic.

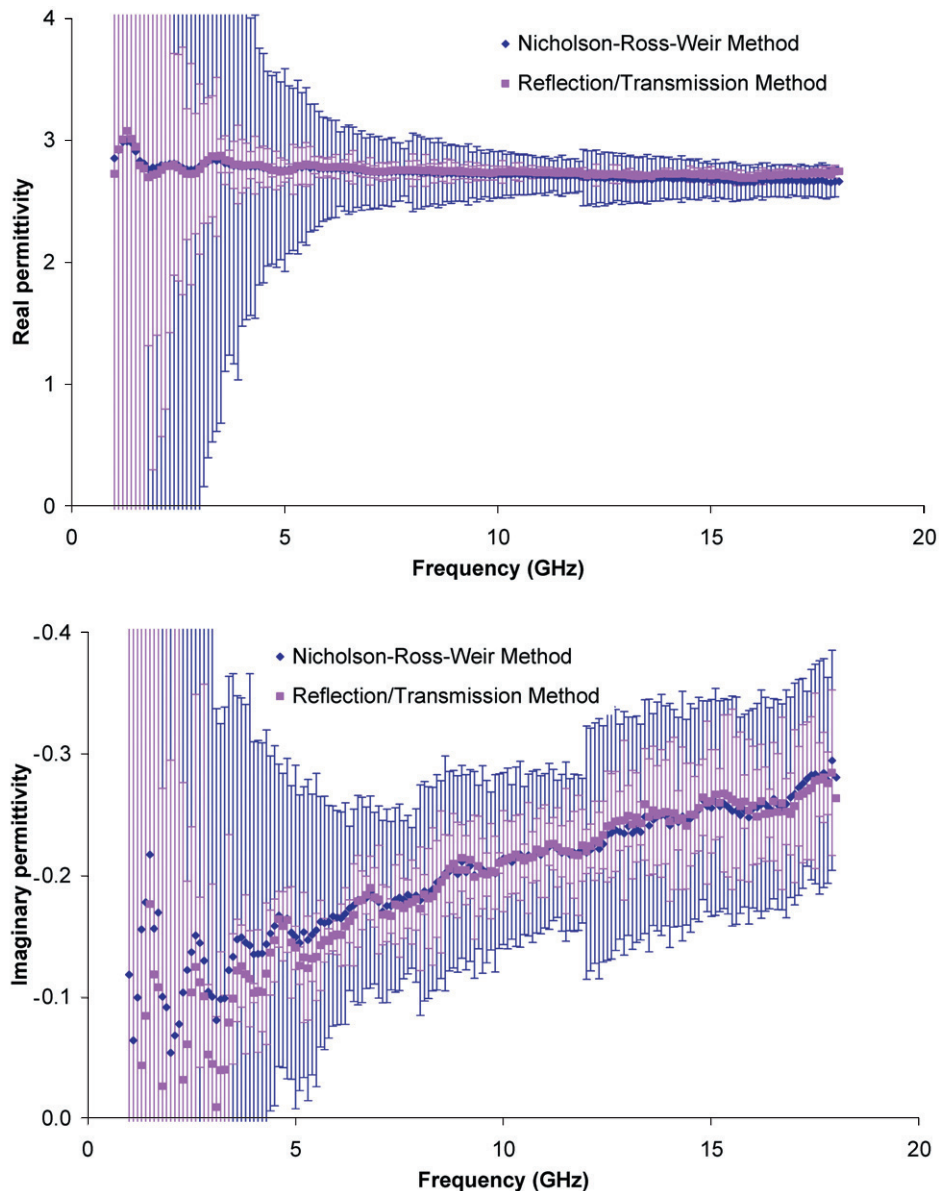


Figure 2. Real and imaginary components of the permittivity for 10 vol% composite, derived from measured reflection and transmission coefficients with (RT method) and without (NRW method) the assumption that the material is non-magnetic.

data, and this is attributed to residual mis-matches after calibration that occur when the sample cell is reconnected to the test-port cables between measurements. Nevertheless, this ‘connector-repeatability’ has been included in the uncertainty budget and it is observed that the magnitude of the ripple is indeed smaller than the quoted measurement uncertainty.

Figures 2 and 3 present the measured dielectric response of composites with low and high filler concentrations (10 and 50 vol%) to provide an indication of typical measurement uncertainties achieved with the NRW and RT methods. In most cases, making the assumption that the composites are non-magnetic enables a reduction in measurement uncertainty, with the exception of the uncertainty in the imaginary component at high filler concentrations. Figure 4 presents the measured magnetic response for the same composites derived using the NRW method. This serves to demonstrate the validity of

making the non-magnetic assumption, although it is noted that there is possibly a small diamagnetic effect at the highest filler concentrations. Nevertheless, this is very small compared with the diamagnetic effect previously observed in silver-coated micro-sphere-filled composites [3], and it could equally be attributed to covariance between permittivity and permeability inherent to the NRW method. Hence, the RT method has been used in all subsequent experimental data.

Figure 5 presents the measured dielectric response of the composites over the frequency ranges 1–18, 33–40 and 40–60 GHz. There is clear evidence of a dielectric relaxation covering the measured frequency range, both from the dispersive nature of the (frequency dependent) real permittivity and the increasing loss shown by the imaginary component of the permittivity over the frequency range 1–18 GHz. The existence of a loss peak becomes more obvious as the filler

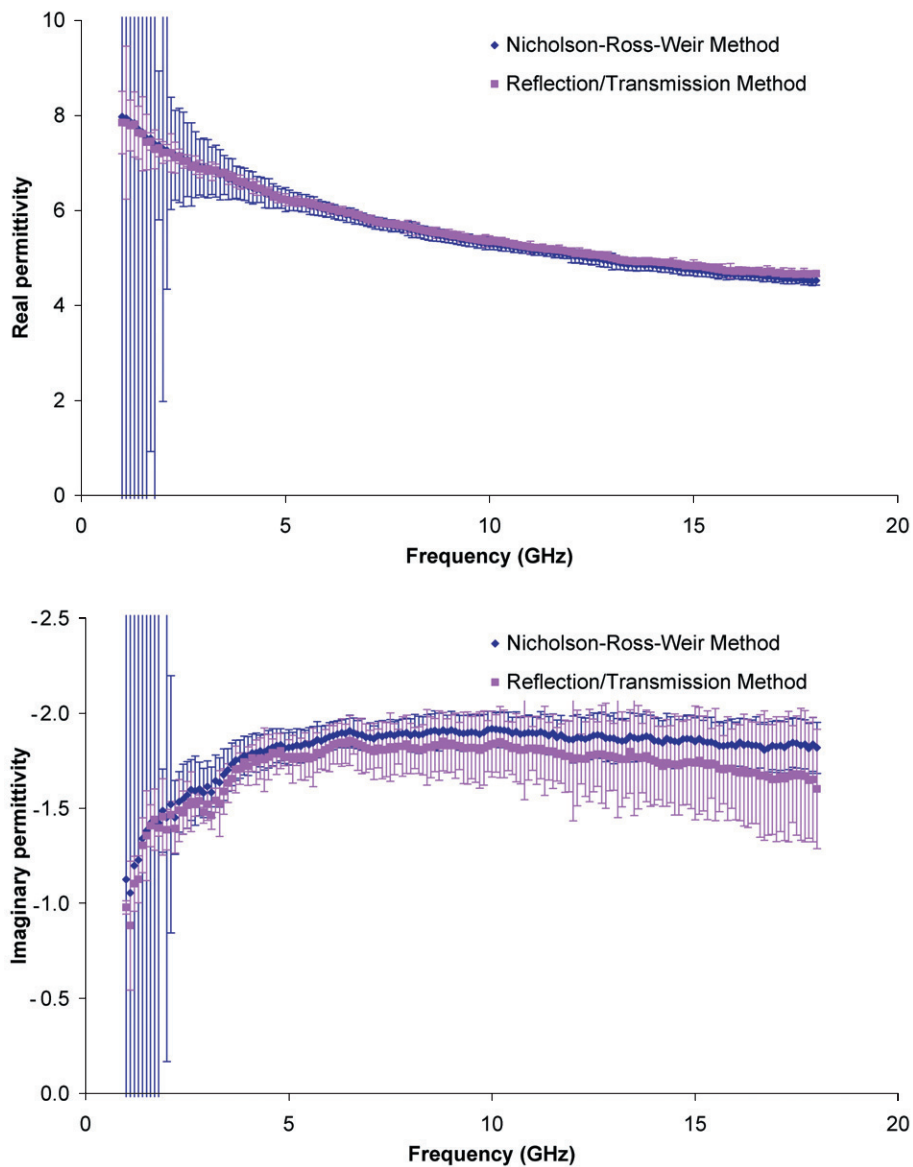


Figure 3. Real and imaginary components of the permittivity for 50 vol% composite, derived from measured reflection and transmission coefficients with (RT method) and without (NRW method) the assumption that the material is non-magnetic.

concentration is increased (this is consistent with effective medium theory as will be demonstrated in section 4) with a maximum value visible for filler concentrations in excess of 30 vol%. The higher frequency, 33–60 GHz, data help us to bound the relaxation process by providing evidence of decreasing loss (again shown by the imaginary component of the permittivity) above the relaxation frequency. It is noted that this is despite the increased challenge for obtaining good quality test results at these higher frequencies and the existence of systematic shifts in the data between the two frequency ranges for the reasons stated in section 2. Both data sets support the observation that the limiting high frequency permittivity (above the relaxation) and the relaxation amplitude increase with increasing filler concentration, as expected [5].

Most interestingly, these experimental results demonstrate a dramatic reduction in the relaxation frequency, by approximately five orders of magnitude, compared with that

expected for similar composites with solid tungsten particles exhibiting bulk conductivity. This aspect will now be explored using effective medium theory in sections 4 and 5.

4. Effective dielectric properties

4.1. Background

The *effective* dielectric properties of composite materials have been of scientific and engineering interest for many years, dating back to at least the times of Lord Rayleigh [18] and Maxwell [19]. ‘Effective medium theories’ (EMTs) or mixture laws are used to predict the properties of a composite from those of its components. The theories or models grouped under this category are numerous [5, 20] and they continue to attract much interest due to the mathematical simplicity with which dielectric properties can be optimized. The classical basis of a number of these models is the Clausius–Mossotti model for the

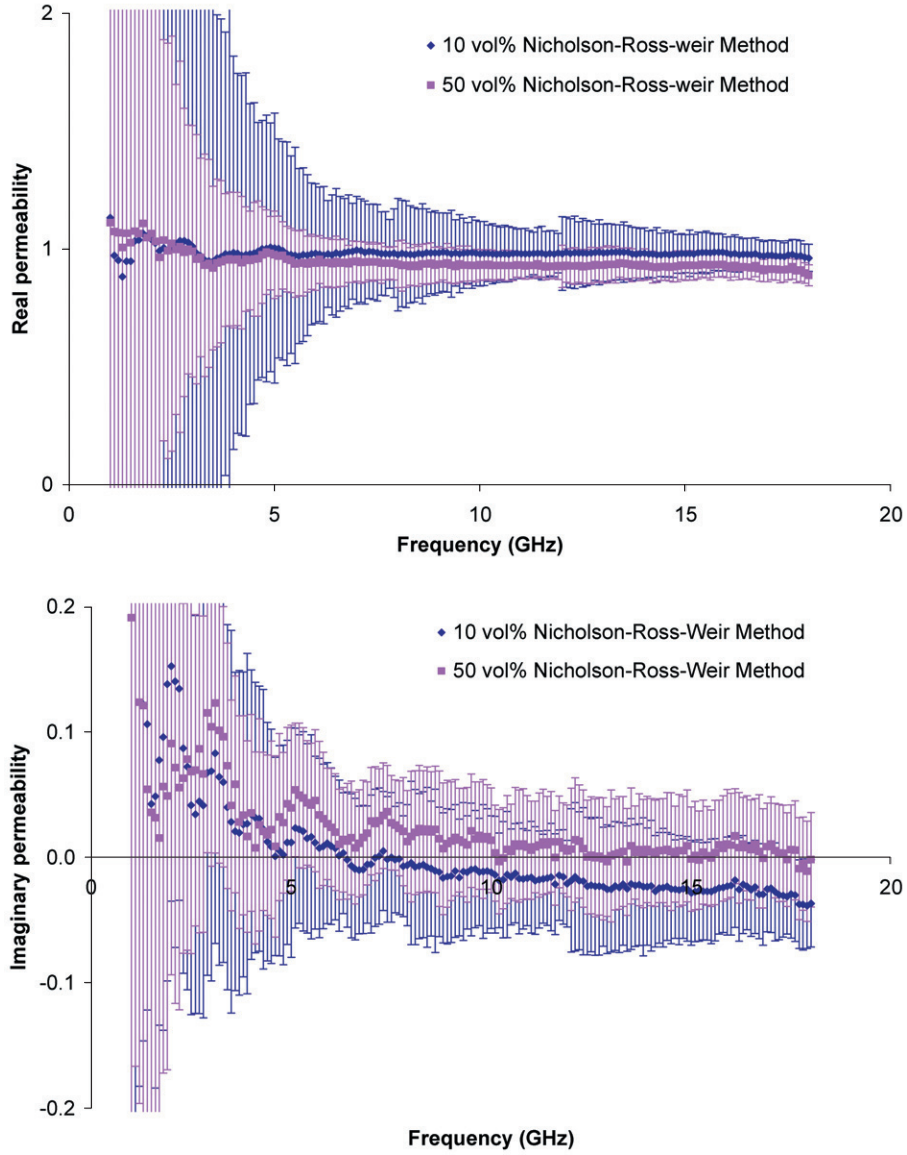


Figure 4. Real and imaginary components of the permeability for 10 and 50 vol% composites, derived from measured reflection and transmission coefficients using the NRW method (i.e. without the assumption that the materials are non-magnetic).

local field, the result of which is reproduced here as equation (1) (with ε the permittivity of the medium, ε_0 the permittivity of free space, α_n ($n = 1, 2, \dots$) the polarizabilities of the different dipoles contained in the medium and N_n the number of dipoles (of polarizability α_n) per unit volume)

$$\frac{\varepsilon - 1}{\varepsilon + 2} = \frac{1}{3\varepsilon_0} \sum_n N_n \alpha_n. \quad (1)$$

It is noted that the polarizable species in this model are assumed to reside in free space. If this is not the case and the background medium has a permittivity ε_b , then equation (1) becomes

$$\frac{\varepsilon - \varepsilon_b}{\varepsilon + 2\varepsilon_b} = \frac{1}{3\varepsilon_0} \sum_n N_n \alpha_n. \quad (2)$$

Two of the most popular EMTs are derived from this equation by using the Clausius–Mossotti model to provide expressions for the permittivity of the individual components (termed

matrix and filler here, with intrinsic permittivities ε_m and ε_f). It can thus be shown that the following generic formula can be derived by expanding the right-hand side of equation (2) in terms of the expressions for the permittivities of these two constituent materials and replacing the number density of the polarizable species with the volume fractions of the constituents (v_m and v_f).

$$\frac{\varepsilon - \varepsilon_b}{\varepsilon + 2\varepsilon_b} = v_m \frac{\varepsilon_m - \varepsilon_b}{\varepsilon_m + 2\varepsilon_b} + v_f \frac{\varepsilon_f - \varepsilon_b}{\varepsilon_f + 2\varepsilon_b}. \quad (3)$$

The construction of equation (3) embodies a critical assumption common in most EMTs: that the polarizabilities of adjacent filler particles are uncoupled. This implies that the mixture is dilute. In addition to the dilute filler approximation, limitations are also incurred because of the use of specific filler particle shapes and spatial arrangements to permit analytic solutions. (Indeed, the derivation of equation (3) represents the

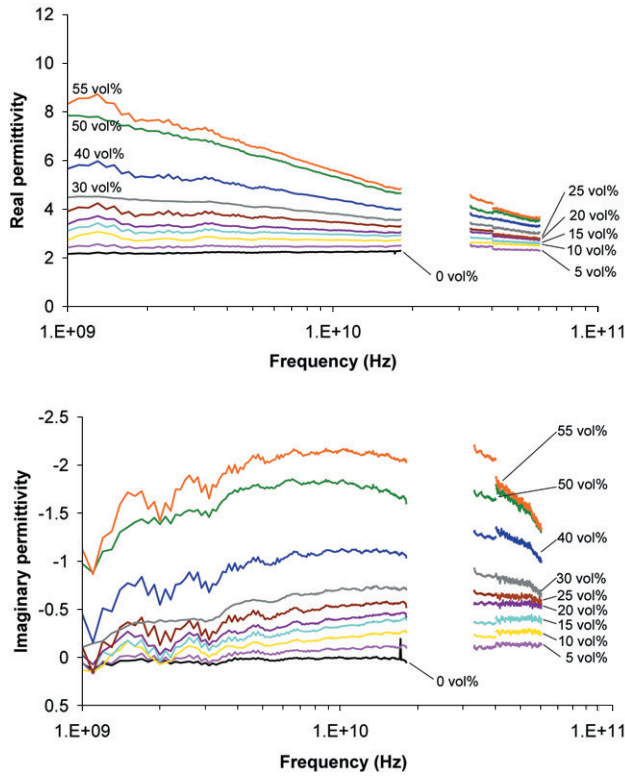


Figure 5. Measured real and imaginary components of the permittivity for composites with filler concentration in the range 0–55 vol% over the frequency ranges 1–18, 33–40 and 40–60 GHz.

case of spherical particles.) For example, the Rayleigh mixture formula follows by setting the permittivity of the background medium equal to that of the matrix ($\epsilon_b = \epsilon_m$). Explicitly,

$$\frac{\epsilon - \epsilon_m}{\epsilon + 2\epsilon_m} = v_f \frac{\epsilon_f - \epsilon_m}{\epsilon_f + 2\epsilon_m}. \quad (4)$$

On the other hand, the (symmetric) Bruggeman EMT is obtained from equation (3) by applying the condition of self-consistency, that is, by setting the permittivity of the background medium equal to the required or resulting effective permittivity of the composite ($\epsilon_b = \epsilon$). Despite the assumptions, the Rayleigh and symmetric Bruggeman models form a good basis for exploring the effective properties of conducting-particle-filled composites. The former is appropriate for isolated particle microstructures and is most relevant to the experimental results presented in this paper. The latter is appropriate when particles have a tendency to agglomerate, forming clusters and connected networks [3].

The effective properties of a conducting-particle-filled composite as a function of filler concentration and frequency may be obtained by solving equation (4) after substituting for the matrix and filler permittivities (which will typically be complex). In Maxwell–Garnett form, equation (4) is written

$$\epsilon = \epsilon_m + 3\epsilon_m \frac{S}{1 - S}, \quad (5)$$

wherein

$$S = v_f \frac{\epsilon_f - \epsilon_m}{\epsilon_f + 2\epsilon_m}. \quad (6)$$

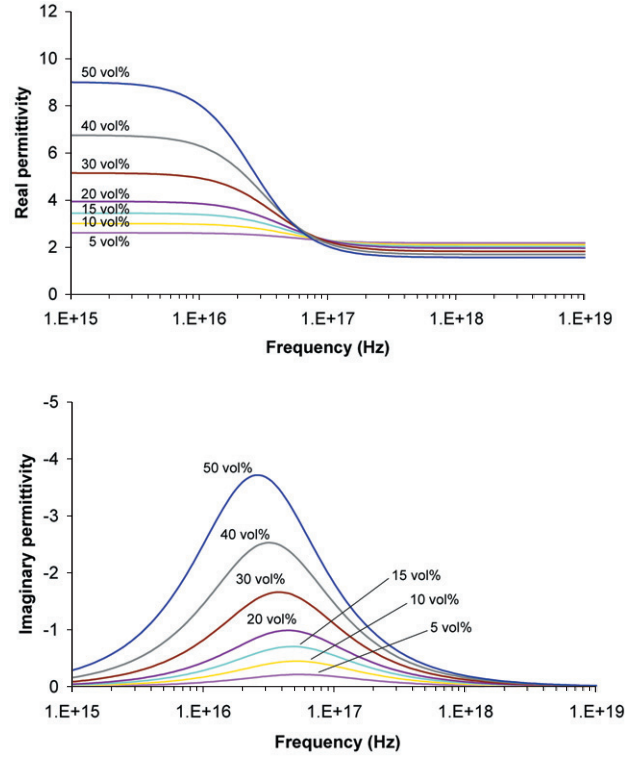


Figure 6. Real and imaginary components of the permittivity calculated using the Maxwell–Garnett EMT for paraffin wax filled with solid tungsten particles exhibiting bulk conductivity.

In general, it will not be a severe approximation to treat the matrix permittivity as frequency independent, unless the specific matrix material has intrinsic molecular processes that give rise to their own dielectric relaxation response in the frequency range of interest. For paraffin wax, over the frequency range of interest here, no such processes exist; hence, the value of the permittivity at 10 GHz given in section 3 will be used in all calculations presented. The permittivity of conducting particles at microwave (or lower) frequencies can be approximated from the Drude model in terms of the bulk dc conductivity of the conductor (σ_f) and the angular frequency ($\omega = 2\pi f$) [21]. This approximation is valid for $\omega\epsilon' \ll \sigma$ and is given by equation (7)

$$\epsilon_f = 1 - j \frac{\sigma_f}{\omega\epsilon_0}. \quad (7)$$

Figure 6 presents the effective real and imaginary components of the permittivity for paraffin wax filled with solid tungsten particles exhibiting bulk conductivity over the concentration range 5–50 vol% and calculated using equations (5) to (7). Figure 7 presents the variation of relaxation frequency and relaxation amplitude with filler concentration, confirming the trends observed in the experimental data, figure 5. However, there is a massive difference of at least six orders of magnitude between the predicted and measured relaxation frequencies. Clearly, the particles under investigation are not behaving as solid tungsten particles.

4.2. Multi-layer particles

The next step is to consider the influence of the coated particle geometry on the relaxation frequency. The analysis used here

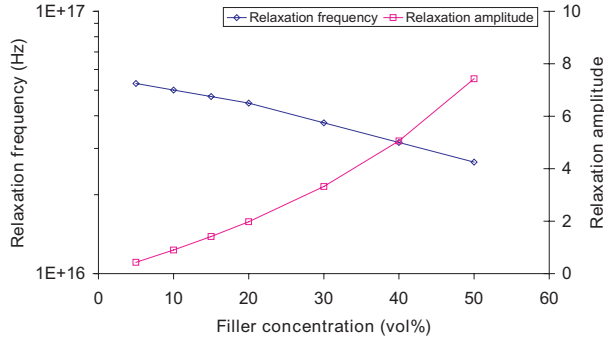


Figure 7. Filler concentration dependence of relaxation frequency and amplitude for the data presented in figure 6.

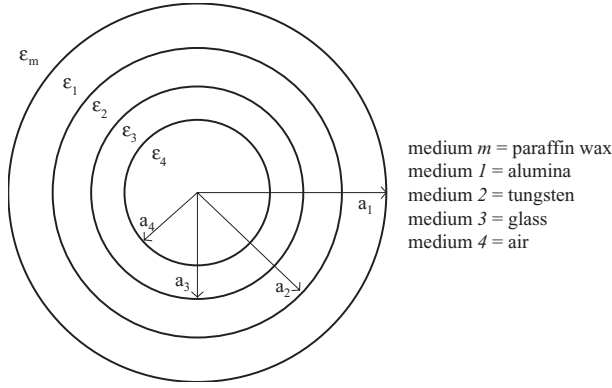


Figure 8. Geometry of four-layer particle.

is that of Sihvola and Lindell for an N -layer spherical filler particle, in which the Rayleigh mixing formula is generalized to deal with layered filler particles [22]. In the case of a four-layer particle, figure 8, the result is

$$\frac{\varepsilon - \varepsilon_m}{\varepsilon + 2\varepsilon_m} = v_f \frac{(\varepsilon_1 - \varepsilon_m) + (2\varepsilon_1 + \varepsilon_m)g_4(\varepsilon_i, a_i)}{(\varepsilon_1 + 2\varepsilon_m) + 2(\varepsilon_1 - \varepsilon_m)g_4(\varepsilon_i, a_i)}, \quad i \in [1, 4]$$

$$g_4 = \left\{ (\varepsilon_2 - \varepsilon_1) \left(\frac{a_2^3}{a_1^3} \right) + (2\varepsilon_2 + \varepsilon_1) \left\{ \left[(\varepsilon_3 - \varepsilon_2) \left(\frac{a_3^3}{a_1^3} \right) + (2\varepsilon_3 + \varepsilon_2) \frac{(\varepsilon_4 - \varepsilon_3)(a_4^3/a_1^3)}{\varepsilon_4 + 2\varepsilon_3} \right] \left[(\varepsilon_3 + 2\varepsilon_2) + 2(\varepsilon_3 - \varepsilon_2) \times \frac{(\varepsilon_4 - \varepsilon_3)(a_4^3/a_3^3)}{\varepsilon_4 + 2\varepsilon_3} \right]^{-1} \right\} \left\{ (\varepsilon_2 + 2\varepsilon_1) + 2(\varepsilon_2 - \varepsilon_1) \times \left[(\varepsilon_3 - \varepsilon_2) \left(\frac{a_3^3}{a_2^3} \right) + (2\varepsilon_3 + \varepsilon_2) \frac{(\varepsilon_4 - \varepsilon_3)(a_4^3/a_2^3)}{\varepsilon_4 + 2\varepsilon_3} \right] \right\} \left[(\varepsilon_3 + 2\varepsilon_2) + 2(\varepsilon_3 - \varepsilon_2) \frac{(\varepsilon_4 - \varepsilon_3)(a_4^3/a_3^3)}{\varepsilon_4 + 2\varepsilon_3} \right]^{-1} \right\}^{-1} \right\} . \quad (8)$$

Figure 9 compares the result from using equation (8) for a 50 vol% particle concentration, assuming that the 20 nm thick tungsten layer retains bulk conductivity, with the equivalent result in figure 6 for solid tungsten particles. It is observed that the layered structure itself accounts for approximately half of the downward logarithmic frequency shift in the relaxation frequency towards the experimental value (~ 10 GHz, figure 5). It is also noted that the relaxation amplitude is slightly reduced

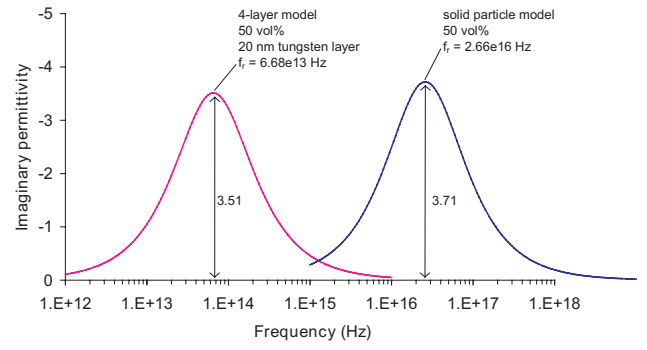


Figure 9. Imaginary permittivity calculated using a four-layer Sihvola–Lindell EMT for paraffin wax filled with 50 vol% tungsten-coated particles and the Maxwell–Garnett EMT for paraffin wax filled with 50 vol% solid tungsten particles (in both cases the tungsten is assumed to exhibit bulk conductivity).

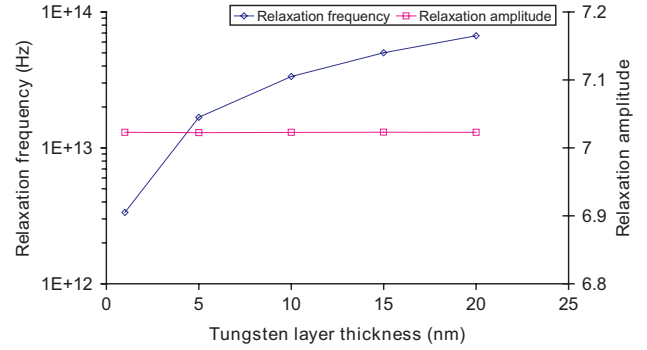


Figure 10. Dependence of relaxation frequency and amplitude on the thickness of the tungsten layer calculated using a four-layer Sihvola–Lindell EMT (all other model parameters as for figure 9).

for the layered particle model. Figure 10 demonstrates how the relaxation frequency and amplitude vary with the thickness of the tungsten layer. It is observed that the relaxation amplitude is invariant with coating thickness over the range 1–20 nm. Moreover, it is concluded that order of magnitude changes in the layer thickness would be required to reduce the relaxation frequency to match the experimental value. Hence, changes in other model parameters are sought to account for the experimental data. The most obvious candidate is the coating conductivity since the relationship between filler conductivity and relaxation frequency is well known [5] and the nano-scale thickness of the tungsten coating may justify a modification to this parameter as the layer thickness approaches the electron mean free path.

Figure 11 compares the result from using equation (8) for a 50 vol% particle concentration, with reduced coating conductivity, with the equivalent experimental data. It is observed that reducing the tungsten conductivity from the bulk value of 1.77×10^7 to 2330 S m^{-1} for the 20 nm thick layer enables a good fit to the experimental relaxation frequency. However, it is clear that the amplitude and width of the relaxation are not well reproduced. It would appear that there is a significant degree of broadening of the relaxation process in the experimental data. Nevertheless, it is concluded that both the thickness and conductivity of the tungsten layer are instrumental in producing the observed reduction in the

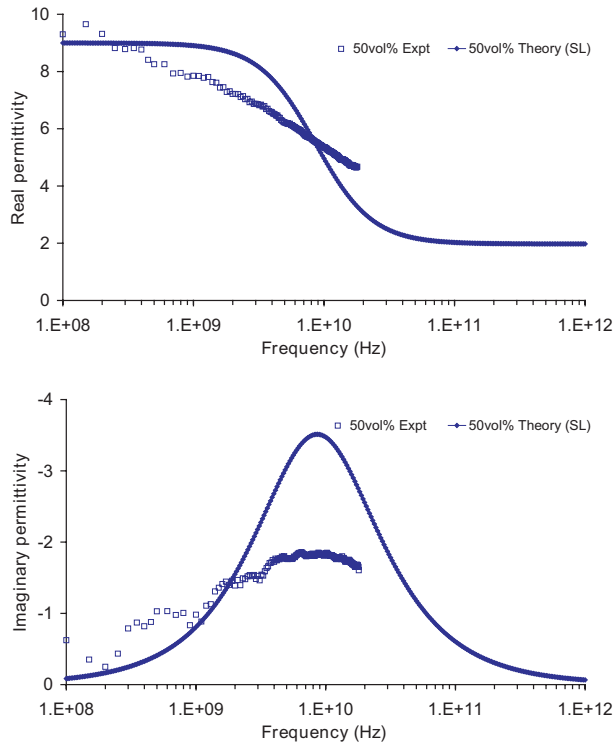


Figure 11. Comparison of measured and calculated real and imaginary components of permittivity for a filler concentration of 50 vol% (calculation with four-layer Sihvola–Lindell EMT and a filler conductivity of 2330 S m^{-1}).

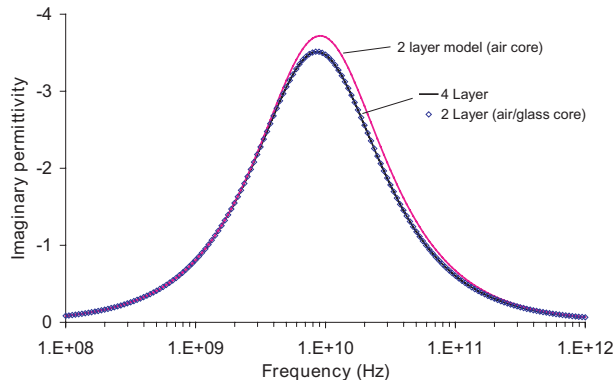


Figure 12. Comparison of imaginary permittivity for a filler concentration of 50 vol% (calculated with varying degrees of approximation using the multi-layer Sihvola–Lindell EMT and a filler conductivity of 2330 S m^{-1}).

relaxation frequency, compared with that of a solid tungsten filler particle of the same size.

4.3. Two-layer simplification

Before considering relaxation broadening mechanisms, it is worth considering the extent to which the multi-layer particle model may be simplified. For instance, is it possible to replace the four-layer model with a two-layer model, arguing that all layers other than the tungsten layer are essentially low-loss dielectrics? Figure 12 demonstrates that it is possible to make a good representation of the four-layer system by using a

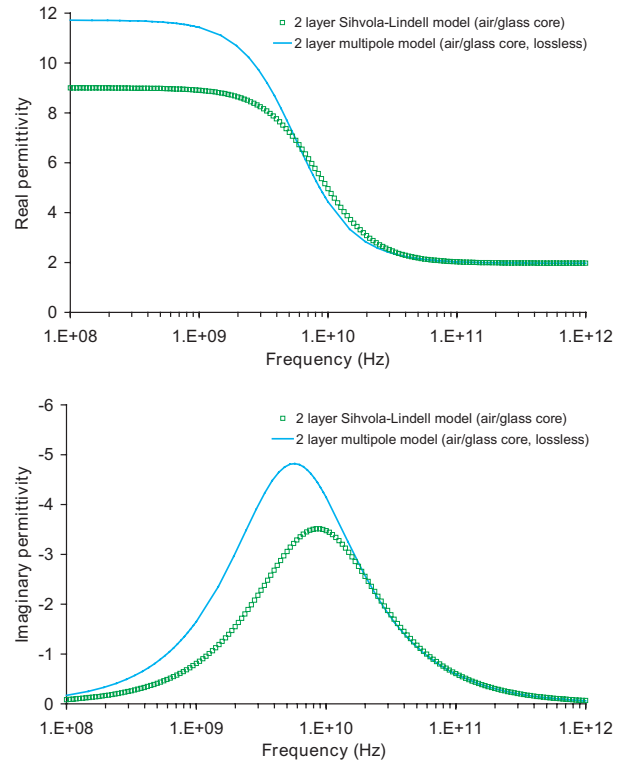


Figure 13. Comparison of real and imaginary components of the permittivity (calculated using a two-layer Sihvola–Lindell EMT and a two-layer multi-pole method for a filler concentration of 50 vol% and a filler conductivity of 2330 S m^{-1}).

two-layer analogue in which the outermost alumina layer is omitted and in which the core is replaced by an effective core whose permittivity has itself been estimated using the Maxwell–Garnett EMT, $\epsilon_{\text{core}} = 1.72 - j(8.3 \times 10^{-3})$ and $a_{\text{core}} = 15 \mu\text{m}$. Sihvola and Lindell’s result for a two-layer particle is given by equation (8), but now g_4 is replaced by

$$g_2 = \frac{\epsilon_2 - \epsilon_1}{\epsilon_2 + 2\epsilon_1} \left(\frac{a_2}{a_1} \right)^3. \quad (9)$$

4.4. Multi-pole contributions

A final point worth considering at this stage is the significance of the inherent assumption that the filler particles are non-interacting (the dilute filler particle approximation). This can be viewed semi-quantitatively by comparing calculations made using equation (8) with those of a multi-pole expansion method in which spherical filler particles are arranged on a simple-cubic lattice [23]. Figure 13 compares calculations for the two-layer particle approximation of those under investigation. The multi-pole model does not account for dielectric losses in the particle core or the matrix phase. However, these are small for the materials used here. The comparison suggests that the Sihvola–Lindell model underestimates both the downward shift in the relaxation frequency and the magnitude of the relaxation amplitude. The level of discrepancy between the two models can be expected to increase with filler concentration. Hence, since the data presented in figure 13 are for a filler concentration of 50 vol%, the comparison presented in the figure represents a reasonable

upper limit to any systematic error introduced by using the Sihvola–Lindell model in this paper.

5. Relaxation broadening

5.1. Mechanisms

First, consider which of the model parameters may be better represented by a distribution of values rather than being single-valued or represented by a mean value. For example, it is apparent from the manufacturer’s literature [9] that the core S60 particles exhibit a distribution of radii, quantified in table 1. This is also clear from a micrograph, figure 14 [8], showing the coated particles. The tungsten coating thickness also varies somewhat [8] as a consequence of the coating process, in which the core particles are tumbled in vacuum while being sputter coated with tungsten vapour [7]. Variations in the coating thickness itself may give rise to relaxation broadening. In addition, variations in the tungsten conductivity in these nano-scale coatings, due to variations in the coating thickness, are likely to contribute to relaxation broadening. The filler particle concentration is also likely to be locally variable, but this effect is not considered here since the model deals with macroscopic averages. Finally, it is possible that inter-particle interactions provide a further broadening mechanism, but these will not be considered here. (For the interested reader, Barrera *et al* [24] have considered such a situation in terms of dipolar fluctuations, introducing a renormalized polarizability to the Maxwell–Garnett EMT.)

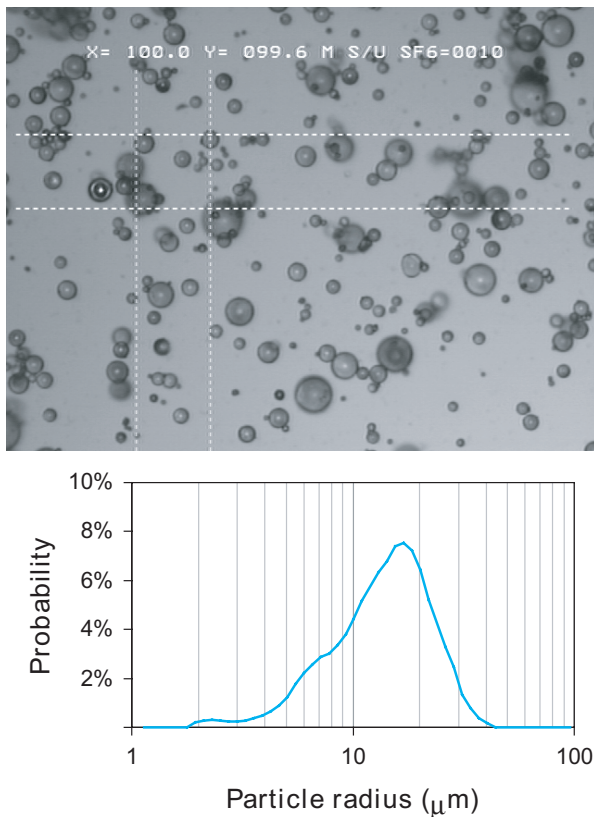


Figure 14. Micrograph and measured particle size distribution of coated particles. The marked square in the micrograph is $100\ \mu\text{m} \times 100\ \mu\text{m}$.

5.2. The effect of particle size distributions

A number of researchers have considered the effect of particle size distributions on the effective dielectric properties of composites. Barrera *et al* [25] demonstrate a broadening of absorption peaks compared with that predicted using Maxwell–Garnett EMT. Spanoudaki and Pelster [26] show that the filler concentration dependence changes from following the Maxwell–Garnett EMT for monodisperse fillers to following the Hanai–Bruggeman EMT [27] for broad particle size-distributions. However, Fu *et al* [28] highlight that the Hanai–Bruggeman result is inconsistent with an approach that includes critical multi-pole terms that are non-zero for non-spherically symmetric size distributions.

The particle size distribution of the coated particles, measured using a Microtrac standard range particle analyser, is shown in figure 14. The distribution is not well represented by either a normal or a log-normal distribution, but it is nevertheless broad and consistent with the manufacturer’s data for the core S60 particles. Therefore, let us first consider the use of the Hanai–Bruggeman EMT to fit the experimental data. Adapting Hanai’s derivation [27] for coated filler particles yields the following relation

$$\left(\frac{\varepsilon - \beta_2 \varepsilon_1}{\varepsilon_0 - \beta_2 \varepsilon_1}\right) \left(\frac{\varepsilon_0}{\varepsilon}\right)^{1/3} = 1 - v_f, \quad (10)$$

$$\beta_2 = \frac{\varepsilon_2 + 2\varepsilon_1 + 2(a_2/a_1)^3(\varepsilon_2 - \varepsilon_1)}{\varepsilon_2 + 2\varepsilon_1 - (a_2/a_1)^3(\varepsilon_2 - \varepsilon_1)}.$$

Figure 15 compares the Hanai–Bruggeman result for a filler concentration of 50 vol% with the experimental data and the Sihvola–Lindell calculation. This model inherently assumes

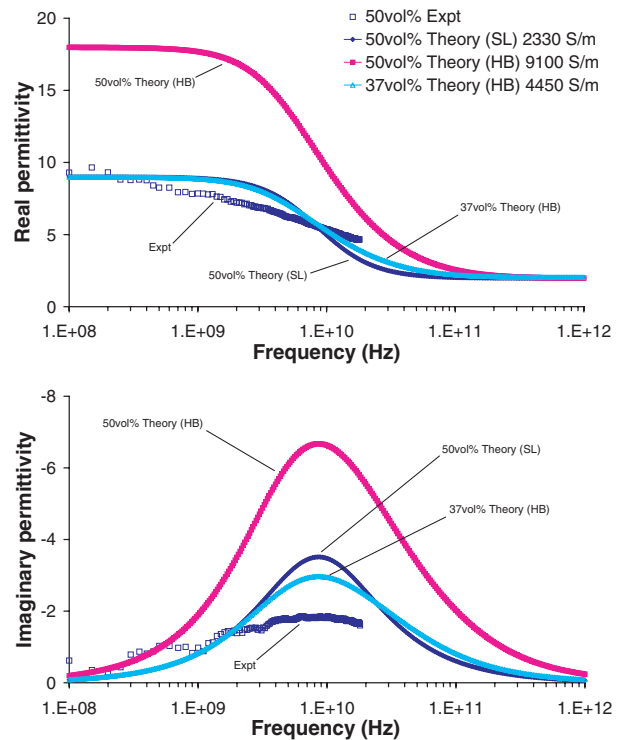


Figure 15. Comparison of Hanai–Bruggeman predictions for 50 vol% filler concentration with Sihvola–Lindell prediction (see figure 11) and experimental data.

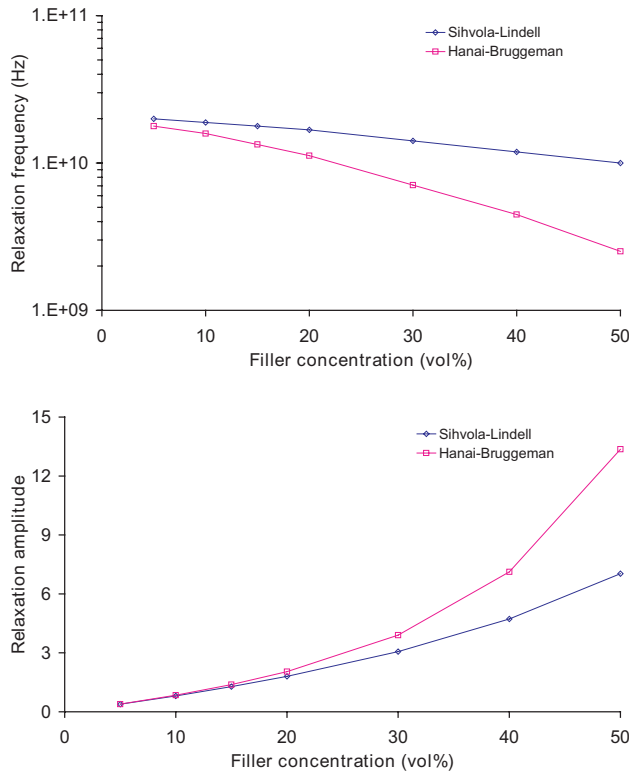


Figure 16. Comparison of filler concentration dependence of relaxation frequency and amplitude for Sihvola–Lindell and Hanai–Bruggeman models for a representative coating conductivity of 2700 S m^{-1} .

a constant ratio of coating thickness to particle radius and predicts a relaxation with greater amplitude. It is further noted that the coating conductivity is increased to maintain a fit to the experimental relaxation frequency. It is only possible to reduce the relaxation amplitude by artificially reducing the filler concentration. Figure 15 demonstrates that reducing the filler concentration to 37 vol% enables a close match to the dispersion predicted by the Sihvola–Lindell model for the real permittivity, whilst also broadening the loss peak.

To complete the comparison of the Sihvola–Lindell and Hanai–Bruggeman models, figure 16 compares the dependence of the relaxation frequency and relaxation amplitude on filler concentration. It is observed that the Hanai–Bruggeman model predicts a greater rate of reduction in the relaxation frequency with increasing filler concentration, coupled with a greater rate of increase in the relaxation amplitude. However, returning to the comparison with experimental data given in figure 15, it is concluded that broadening due to a particle size distribution is not a significant feature in the experimental data because the real permittivity is not sufficiently enhanced for frequencies below the relaxation frequency.

5.3. The effect of coating thickness distributions

Reverting to the Sihvola–Lindell formalism, given for a four-layer filler particle in equation (8), relaxation broadening due to a distribution of coating thickness is now considered. Recalling the outcome of section 4.3, it is computationally

simpler to proceed with a two-layer analogue filler particle, equation (9). In order to introduce a coating thickness distribution, rewrite the result of equation (9) assuming n spherical particles dispersed in a total volume V . Also expand the filler volume fraction to reveal its dependence on the filler particle radius. Then,

$$\frac{\varepsilon - \varepsilon_m}{\varepsilon + 2\varepsilon_m} = \frac{4\pi n a_1^3}{3V} \frac{(\varepsilon_1 - \varepsilon_m) + (2\varepsilon_1 + \varepsilon_m)g_2(\varepsilon_i, a_i)}{(\varepsilon_1 + 2\varepsilon_m) + 2(\varepsilon_1 - \varepsilon_m)g_2(\varepsilon_i, a_i)}, \quad (11)$$

$$i = 1, 2.$$

If now the layer thickness on the particle changes but the core radius remains fixed, a_1 in equation (11) changes but a_2 remains constant. It is convenient to make the substitution $a_1 = a_2 + t$, with t being the coating thickness. For a continuous distribution of t , it is possible to replace the right-hand side of equation (11) with an integral (sum) over all t following the reasoning adopted by Sihvola and Lindell for the derivation of their equation (39) in [22]. The underpinning assumption is that the filler particles are uncorrelated, residing in a background medium with permittivity ε_m . Rearranging equation (11) in Maxwell–Garnett form leads to the following expression for the effective permittivity of a dispersion of monodisperse coated particles with a distribution of coating thickness:

$$\varepsilon = \varepsilon_m + 3\varepsilon_m \frac{S}{1 - S},$$

$$S = \frac{4\pi}{3V} \int_0^\infty p(t)(a_2 + t)^3 \times \frac{(\varepsilon_1 - \varepsilon_m)(\varepsilon_2 + 2\varepsilon_1)(a_2 + t)^3 + (2\varepsilon_1 + \varepsilon_m)(\varepsilon_2 - \varepsilon_1)a_2^3}{(\varepsilon_1 + 2\varepsilon_m)(\varepsilon_2 + 2\varepsilon_1)(a_2 + t)^3 + 2(\varepsilon_1 - \varepsilon_m)(\varepsilon_2 - \varepsilon_1)a_2^3} dt, \quad (12)$$

where $p(t)$ is the probability of a coating having thickness t . Assuming a normal (or Gaussian) distribution of t leads to the following expression for $p(t)$:

$$p(t) = \frac{1}{\sigma\sqrt{2\pi}} \exp\left(-\frac{1}{2}\left(\frac{t - \bar{t}}{\sigma}\right)^2\right), \quad (13)$$

where \bar{t} is the mean value of t and σ is the standard deviation. A normal distribution of t gives rise to a finite probability of a coating thickness less than zero, which cannot be permitted physically. Cutting off the normal distribution at $t = 0$, as in equation (12), implies that

$$\int_0^\infty p(t) dt < 1. \quad (14)$$

Explicit normalization of S , to account for the fact that the integral over the probability distribution is less than unity, is not necessary, however, since the expression for V in terms of $p(t)$ is also cut off at $t = 0$,

$$V = \frac{4\pi}{3v_f} \int_0^\infty p(t)(a_2 + t)^3 dt. \quad (15)$$

Figure 17(a) shows how the relaxation frequency first decreases, with increasing standard deviation in the layer thickness distribution, until the lower limit of zero thickness is reached when the standard deviation is approximately half of the mean coating thickness. This behaviour is consistent

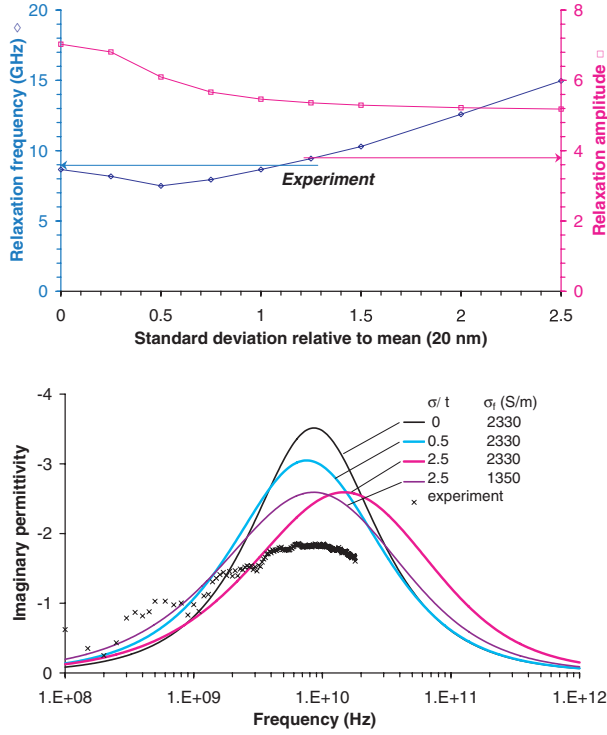


Figure 17. (a) The influence of a distribution of coating thickness on the relaxation peak frequency and amplitude for a mean coating thickness of 20 nm. (b) Comparison of predicted relaxation peak with experiment for selected thickness distributions with a mean thickness of 20 nm and specified coating conductivity.

with the definition that 95% of coatings have a thickness in the range $\bar{t} \pm 2\sigma$. For broader thickness distributions the relaxation frequency increases with increasing standard deviation. The relaxation amplitude is observed to decrease rapidly until the standard deviation equals the mean thickness, and then the rate of decrease in the relaxation amplitude tends to zero. Figure 17(b) presents some calculated examples of the relaxation peak in the frequency domain for a filler concentration of 50 vol%, for various values of σ and coating conductivity. As σ increases, the coating conductivity must be reduced to maintain a match between the predicted and experimental relaxation frequency. The relaxation peak broadens and is reduced in amplitude, improving the fit between theory and experimental data. However, the fact that the rate of decrease in the relaxation amplitude tends to zero as σ increases (figure 17(a) means that a further source of broadening must be sought in order to better fit the relaxation amplitude of the experimental data.

5.4. Influence of the nano-scale

The analysis presented so far has assumed that a greatly reduced tungsten conductivity is necessary and realistic in accounting for a significant degree of downward shift in the relaxation frequency. In this section we consider the justification for this assumption by reviewing the validity of representing the permittivity of the tungsten coating with a low frequency approximation of the Drude model. The Drude

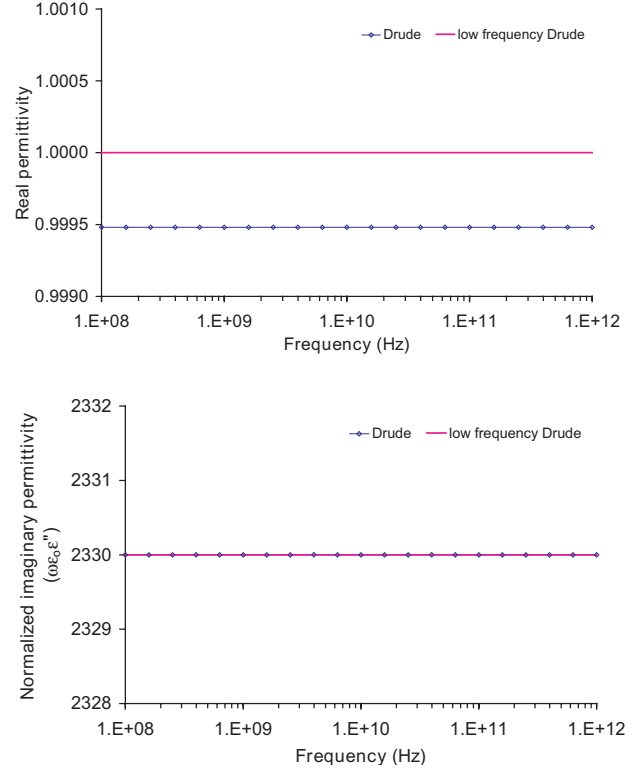


Figure 18. Demonstration of the validity of the low frequency Drude approximation for the permittivity of the tungsten coating across the frequency range 0.1–1000 GHz.

model is more normally given by equation (16),

$$\epsilon_f = 1 - \frac{\omega_p^2}{\omega(\omega - j/\tau)}, \quad (16)$$

where ω_p is the plasma frequency and τ is the electronic relaxation time. Representative values for the parameters appearing in equation (16) are quoted in table 1, for bulk tungsten. Figure 18 compares the real and imaginary components of the permittivity of tungsten obtained from equations (7) and (16) when σ_f and τ , respectively, have been adjusted to fit the relaxation frequency of the experimental data for a filler concentration of 50 vol%. It is observed that the real component differs by less than 0.1% and that the imaginary components are identical. Hence, the figure demonstrates the validity of using the low frequency approximation in this work. In the low frequency model, σ_f has been multiplied by a factor of approximately 1.3×10^{-4} to achieve a fit. In the full-Drude model, $\tau = \tau_{\text{bulk}}$ (as given in table 1) has been multiplied by the same factor to achieve a fit. This adjustment represents a very significant reduction in the mean time between electron scattering events.

It is worth pursuing the detailed representation of the tungsten permittivity further to explore the physical origins of the reduced relaxation time. The next step is to consider the appropriate conduction electron scattering mechanisms. As the physical thickness of the tungsten coating is reduced to the nano-scale, the thickness approaches the bulk electron mean free path ($l_{\text{bulk}} = v_F \tau_{\text{bulk}}$, v_F being the Fermi velocity), estimated as 14 nm for tungsten. Under such conditions surface

scattering of the conduction electrons can occur. Alternatively, electron scattering can occur due to presence of impurities or even defects in such thin coatings. Hence, additional relaxation times associated with these extra processes will contribute to the overall response. Provided the separate processes are independent of one another, a new overall relaxation time is defined by following Matthiessen's rule [29]:

$$\frac{1}{\tau} = \frac{1}{\tau_{\text{bulk}}} + \frac{1}{\tau_1} + \dots \quad (17)$$

In equation (17) it is implicitly assumed that the plasma frequency and the Fermi velocity remain unchanged. Surface scattering is introduced in this way by many authors [25,30,31], through a size dependent term as shown in equation (18):

$$\frac{1}{\tau} = \frac{1}{\tau_{\text{bulk}}} + A \frac{v_F}{l_{\text{path}}}, \quad (18)$$

where A is a parameter that represents the degree of chemical interaction between the matrix material and the conduction electrons in the metal [31] and l_{path} is the mean free path. The minimum value of A reported in references [25,30,31] is 0.25 for silver particles in vacuum, and it is observed that A increases with the level of interaction.

For solid nano-particles the mean free path is generally taken to be the particle radius, but for metallic shells the following expression has been proposed [32]. Using the notation for our two-layer particles,

$$l_{\text{path}} = \sqrt[3]{(a_1 - a_2)(a_1^2 - a_2^2)}, \quad (19)$$

yielding a value of 229 nm in this case. If it is assumed that the mean free path is constrained between this value and the coating thickness, then the effective relaxation time lies in the range $0.58 \leq \tau/\tau_{\text{bulk}} \leq 0.94$, assuming $A = 1$.

Taking the best case, that the mean free path equals the coating thickness, and representing the permittivity of tungsten in equation (12) and equation (16) with (18) and (19), it is possible to explore whether any further broadening occurs through the inclusion of the coating thickness in the expression for the coating permittivity. Figure 19 demonstrates that reducing the mean coating thickness to 10 nm with a standard deviation of 13 nm can yield a very close fit to the experimental data if the parameter A is permitted to vary freely. Here, $A = 4500$, orders of magnitude greater than we have seen elsewhere in the literature [25,30,31]. Such a value is justified by noting that it simply reflects the presence of stronger free electron scattering than expected from the nominal values (provided by the manufacturer) of the parameters describing the particle geometry and composition. Stronger free electron scattering is plausible since very little is actually known at the present time about the true quality of the nano-scale coating. For comparative purposes, figure 19 also contains a prediction based on equation (12) with the low frequency Drude approximation for the tungsten permittivity, and a prediction assuming no distribution of coating thickness.

To complete the analysis, figure 20 presents fits to experimental data for three filler concentrations spanning the tested range. It is observed that the quality of the fit is good at 50 vol% and acceptable at 15 and 30 vol%. The remaining

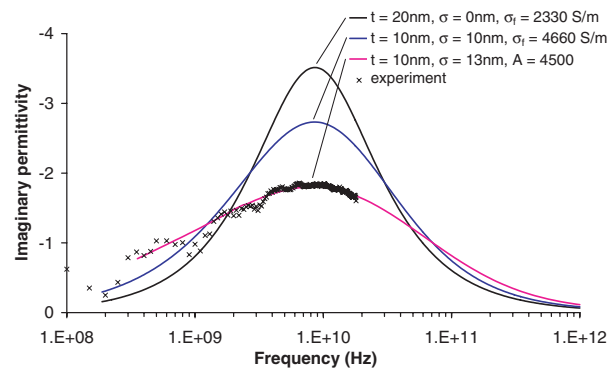


Figure 19. Demonstration that a prediction using a coating thickness distribution (mean thickness = 10 nm, standard deviation = 13 nm) and the full Drude permittivity function for the coating incorporating the nano-scale free electron surface scattering effect (with $A = 4500$) can fit experimental data for a dielectric relaxation peak (for a filler concentration of 50 vol%). Predictions in the absence of a coating thickness distribution and for a coating thickness distribution, but with the coating permittivity represented by the low frequency Drude model, are included for comparison to highlight the successive broadening of the relaxation peak due to the different broadening mechanisms.

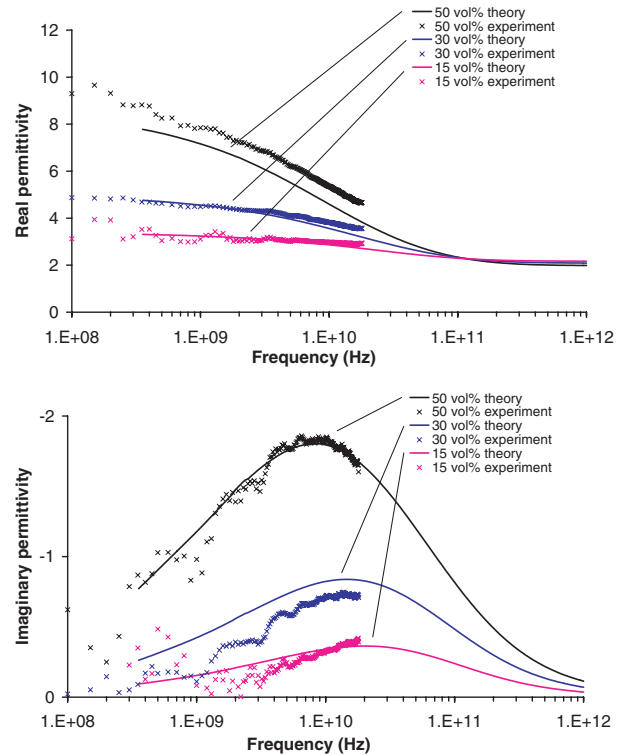


Figure 20. Comparison of fit using a coating thickness distribution (mean thickness = 10 nm, standard deviation = 13 nm) and the full Drude permittivity function for the coating incorporating the nano-scale free electron surface scattering effect (with $A = 4500$) with experimental data for filler concentrations of 15, 30 and 50 vol%.

difference between theory and experiment is considered to be related to inaccuracies in the predicted rate of change of the relaxation frequency with filler concentration. The Sihvola–Lindell model gives too small a rate of change for this system. It is possible that including higher order

multi-pole interaction terms would increase this rate of change and improve the agreement between theory and experiment. Implementation of the renormalization method of Barrera *et al* [24], dealing with inter-particle correlation, could be considered to obtain a further improved fit. An alternative view is that an intermediate position between the Sihvola–Lindell and Hanai–Bruggeman models is needed; in other words, the presence of a particle size distribution acts to increase the rate of change of relaxation frequency with filler concentration. In addition, a preliminary study, in which the tungsten layer is modelled as a two-dimensional percolating network of connected islands, also yields an encouraging fit to the experimental data. Direct observation of the tungsten coating is planned, perhaps using transmission electron microscopy, in order to further develop the model.

6. Conclusions

Through theoretical modelling it can be shown that a composite with nano-scale tungsten-coated filler particles exhibits dielectric relaxation due to interfacial polarization many frequency decades below that of a similar composite with solid metal particles. Experimentally it is observed that the relaxation frequency also occurs several decades below the frequency predicted by theory for a composite with layered filler particles, if a bulk conductivity value for the metal shell is used in the calculation. These observations can be explained by reasoning that the conductivity of the thin metal coating is severely reduced due to nano-scale effects such as reduction of the mean free path of the conduction electrons due to surface scattering [33]. It may be the case that the tungsten coating is not continuous, since similar work on continuous gold nano-shells at optical frequencies does not find a similarly large downward shift in the relaxation frequency [34]. Modelling suggests that the observed broadening of the relaxation is due largely to a distribution of metal coating thickness, and associated distribution of the coating conductivity, rather than the polydispersity of the filler particles. This interpretation is in line with observations on smaller (100–250 nm diameter) metal shells at optical frequencies [34].

Acknowledgments

The authors most gratefully acknowledge the supply of particles and related technical information by Dr Craig Chamberlain of 3M, St Paul, MN, USA. This research was part-funded by the Ministry of Defence as part of the Corporate Research Programme. © QinetiQ Limited 2004. NB's work was performed at the Center for NDE at Iowa State University with funding from the Air Force Research Laboratory through S&K Technologies, Inc. on delivery order number 5007-IOWA-001 of the prime contract F09650-00-D-0018.

References

- [1] Neelakanta P 1995 *Handbook of Electromagnetic Materials* (New York: CRC Press)
- [2] Stauffe D and Aharony A 1994 *Introduction to Percolation Theory* (Philadelphia, PA: Taylor and Francis)
- [3] Youngs I J 2000 *IEE Proc.-Sci. Meas. Technol.* **147** 202
Youngs I 2001 Electrical percolation and the design of functional electromagnetic materials *PhD Thesis* University College, London
- [4] Clerc J, Giraud G, Laugier J and Luck J 1990 *Adv. Phys.* **39** 191–308
- [5] van Beek L K H 1967 *Prog. Dielectrics* vol 7 (London: Iliffe Books Ltd) pp 69–114
- [6] See for example Novocontrol GmbH, <http://www.novocontrol.com/>
- [7] Chamberlain C S, Connell G and Tait W C 1995 *US Patent Specification* 5,389,434
- [8] Chamberlain C S private communication
- [9] 3M product information *Scotchlite™ Glass Bubbles* http://www.3m.com/microspheres/s_k.1.html
- [10] Potter Industries Inc. *Materials Safety Data Sheets for Spherglass® Glass Spheres A-Glass and E-Glass*
- [11] von Hippel A R 1954 *Dielectric Materials and Applications* (New York: Wiley)
- [12] Weast R 1977 *CRC Handbook of Chemistry and Physics* (Ohio: CRC Press)
- [13] Nnolim N, Tyson T and Axe L 2003 *J. Appl. Phys.* **93** 4543–60
- [14] Chakraborty B, Pickett W and Allen P 1976 *Phys. Rev. B* **14** 3227–30
- [15] Clarke R 2003 *A Guide to the Characterisation of Materials at RF and Microwave Frequencies* (London: National Physical Laboratory) (available at <http://www.npl.co.uk/electromagnetic/cem-publications/goodpractice.html>)
- [16] Baker-Jarvis J 1990 *NIST Technical Note* 1341
- [17] Youngs I 2000 *Proc. 8th International Conf. on Dielectric Materials, Measurements and Applications* IEE Conf. Publ. No 473, pp 308–13
- [18] Rayleigh R S 1892 *Phil. Mag.* **34** 481–502
- [19] Maxwell J 1881 *A Treatise on Electricity and Magnetism* (Oxford: Clarendon)
- [20] See for example the following reviews:
Hale D 1976 *J. Mater. Sci.* **11** 2105–40
Aspnes D 1982 *Am. J. Phys.* **50** 704–9
McCullough R 1985 *Comp. Sci. Technol.* **22** 3–21
Priou A 1992 *Dielectric properties of heterogenous materials* (New York: Elsevier)
- [21] Ramo S, Whinnery J and van Duzer T 1984 *Fields and Waves in Communication Electronics* (New York: Wiley)
- [22] Sihvola A H and Lindell I V 1992 *Dielectric Properties of Heterogeneous Materials* ed A Priou (New York: Elsevier) chapter 3 Polarizability modelling of heterogeneous media pp 101–51
- [23] Harfield N 2000 *J. Mater. Sci.* **35** 5809–16
- [24] Barrera R G, Monsivais G and Mochan W 1988 *Phys. Rev. B* **38** 5371
- [25] Barrera R G, Villaseñor-González P, Mochán W L and Monsivais G 1990 *Phys. Rev. B* **41** 7370–6
- [26] Spanoudaki A and Pelster R 2001 *Phys. Rev. B* **64** 64205
- [27] Bruggeman D A G 1935 *Ann. Phys.* **24** 636
Hanai T 1968 *Electrical properties of emulsions Emulsion Science* ed P Sherman (London: Academic)
- [28] Fu L, Macedo P M and Resca L 1993 *Phys. Rev. B* **47** 13818–29
- [29] Ashcroft N and Mermin N 1976 *Solid State Physics* (Philadelphia, PA: Saunders College) chapter 16 Beyond the relaxation time approximation pp 318–28
- [30] Hovel H, Fritz S, Hilger A, Kreibig U and Vollmer M 1993 *Phys. Rev. B* **48** 18178–88
- [31] Oshchepkov S L and Sinyuk A F 1998 *J. Colloid Interface Sci.* **208** 137–46
- [32] Granqvist C and Hunderi O 1978 *Z. Phys. B: Condens. Matter* **30** 47
- [33] Antonets I V, Kotov L N, Nekipelov S V and Golubev Ye A 2004 *Solid-State Electron.* **74** 24–7
- [34] Westcott S L, Jackson J B, Radloff C and Halas N J 2002 *Phys. Rev. B* **66** 155431